J. Fluid Mech. (1996), vol. 319, pp. 197–218

Sound radiation during local laminar breakdown in a low-Mach-number boundary layer

By MENG WANG, SANJIVA K. LELE AND PARVIZ MOIN

Center for Turbulence Research, Stanford University/NASA Ames Research Center, Moffett Field, CA 94035, USA

(Received 9 January 1995 and in revised form 21 March 1996)

The far-field sound of an unstable wave packet undergoing transition in a low-Mach-number, flat-plate boundary layer is investigated in the framework of Lighthill's acoustic analogy. Detailed accounts of the wave packet evolution are obtained by solving the full incompressible Navier–Stokes equations at $Re_{\delta^*} = 1000$. The numerically simulated flow structures show qualitative agreement with experimental observations of the fundamental breakdown type. The acoustic calculations are focused on the quadrupole source functions arising from Reynolds stress fluctuations. The wave packet is shown to produce negligible sound throughout the primary and secondary instability stages. Dramatic amplification of the Reynolds stress quadrupoles occurs as a result of the disintegration of the detached high-shear layer and the associated vortex shedding near the boundary layer edge. The dominant frequency of source oscillations coincides with that of vortex shedding.

1. Introduction

Boundary layer flow transition has long been suggested as a potential noise source in both marine (sonar-dome self-noise) and aeronautical (aircraft cabin noise) applications, owing to the highly transient nature of the process (Farabee, Hansen & Keltie 1989). The design of effective noise control strategies relies upon a clear understanding of the source mechanisms associated with the unsteady flow dynamics during transition. Owing to formidable mathematical difficulties, theoretical treatment of transition noise based on the fundamental equations has been limited to the early linear and weakly nonlinear stages, under simplifying assumptions (Haj-Hariri & Akylas 1986; Akylas & Toplosky 1986).

A powerful alternative for predicting flow-induced sound is the acoustic analogy theory proposed by Lighthill (1952). In this theory, the exact equations for mass and momentum conservation are combined to form a linear, non-homogeneous wave equation for the acoustic density fluctuation, forced by equivalent source terms representing nonlinear flow dynamics in a spatially concentrated region. At low Mach number the source functions can be determined by considering an equivalent incompressible flow, a mathematical approximation justified by Crow (1970) using a singular perturbation procedure. Computational validation of the Lighthill acoustic analogy and related aeroacoustic theories (Powell 1964; Howe 1975; Möhring 1978) has been provided by Mitchell, Lele & Moin (1995), who considered a model problem involving the merging of two co-rotating vortices. Acoustic analogy predictions were

shown to be in excellent agreement with the results computed directly from the compressible Navier–Stokes equations.

Lighthill's theory and its extensions have been used extensively in the study of flow noise from transitional and turbulent boundary layers. According to the developments of Curle (1955) and Powell (1960), fluctuating velocities produce quadrupole sound sources, while fluctuating wall shear stresses take the form of dipole sources. The exact role played by the unsteady surface shear stress is controversial. Landahl (1975) gave an order of magnitude estimate of the turbulent boundary layer noise, based on the Lighthill analogy and a conceptual 'two-scale model' for boundary layer turbulence. He also pointed out the qualitative similarity between the process of breakdown in transition and the bursting phenomenon in a turbulent boundary layer. The dipole radiation was found to be much stronger than the quadrupole radiation at moderate velocities. In contrast, Howe (1979) argued that all the wall shear stress perturbations in the supersonic low-wavenumber range correspond to acoustic waves propagating in the boundary layer, and hence should not be considered as generation terms. Their presence actually diminishes the radiation intensity. Howe's (1979) analysis indicates that at low Mach numbers, the wall-stress effect is in general negligibly small.

Lauchle (1980) considered the intermittent regime in a small-Mach-number boundary layer where flow alternates between laminar and turbulent. The fluctuating wall shear stress, hypothesized as the dominant noise source, is modelled using an intermittency indicator function. The radiated noise spectrum is predicted using Lighthill's analogy. The volume quadrupole contribution is excluded, however, owing to difficulties in modelling the fluctuating Reynolds stresses in the intermittent regime. Lauchle (1981, 1989) and Marboe & Lauchle (1992) later pursued a more ad hoc approach based on the Liepmann analogy (Laufer, Ffowcs Williams & Childress 1964), which postulates that the fluctuation of the boundary layer displacement thickness acts like a piston to the adjacent acoustic medium, giving rise to weak monopole radiation. The intermittency function is again used to model the displacement-thickness fluctuations. A related approach, the 'two-fluids model' (Sornette & Lagier 1984; Lagier & Sornette 1986), also exists and has reviewed by Lauchle (1991) and Marboe & Lauchle (1992).

In the present work, an approach which combines direct numerical simulation of the source field with the Lighthill acoustic analogy is utilized. The transitional boundary layer flow is computed by solving the incompressible Navier–Stokes equations without model assumptions, thus allowing a direct evaluation of the pseudosound as well as the volume acoustic source functions. The latter are used to calculate the radiated pressure field during the transition from primary instability to the laminar breakdown stage. In particular, one is interested in identifying specific flow processes and structures that are effective noise generators. Owing to the neglect of the compressibility effect in the boundary layer simulation, the present study does not give a definitive description of the effect of the unsteady wall shear stress. This issue is discussed briefly in the context of the historical controversy.

Natural transition in a boundary layer starts with modulated Tollmien–Schlichting (T-S) wave trains initiated by random excitations from free-stream turbulence (Gaster 1993). The laminar breakdown process which destroys the smooth, orderly flow pattern is a localized event triggered by instability mechanisms (Kachanov 1994). These observations suggest that, without loss of generality, one could simulate the transition phenomena by following the evolution of a T-S wave packet instead of a periodic wave series as in controlled experiments (e.g. Klebanoff, Tidstrom & Sargent 1962; Kachanov & Levchenko 1984). This results in considerable savings

in computer memory and CPU time due to the reduced domain size. Furthermore, the amplitude modulation allows the wave packet to evolve spontaneously into a turbulent spot, which cannot be achieved if the initial instability wave is strictly periodic (Kachanov 1994). From an acoustic viewpoint, tracking an isolated wave packet has the advantage that the linkage between the calculated sound signal and the specific transition stage is apparent.

The numerical simulation of the transitional boundary layer is a significant part of the present study. However, the sheer volume of literature in this area prevents a thorough review here. A brief overview of relevant works and their relation with the present simulation is deferred to §3.1. The reader is advised to consult two recent review articles (Kleiser & Zang 1991; Kachanov 1994) for additional information.

The presentation is organized as follows. Section 2 outlines the Lighthill acoustic analogy in a rational framework and expresses the far-field asymptotic solution in terms of integrals of near-field source terms. Section 3 describes numerical and physical aspects of wave packet transition, which follows basically the K-type breakdown route: The amplification of two- and three-dimensional instabilities leads to the formation of a streamwise vortex system, or lambda vortex, above which a detached high-shear layer of streamwise velocity is induced. The high-shear layer, susceptible to stronger inflexional instability, creates and sheds eddies of smaller scale as it graduately disintegrates. The computed source field data are used in §4 to evaluate the volume source functions for the far-field acoustic radiation. It is found that the major source of quadrupole sound is the production of the instantaneous Reynolds stress during the high-shear-layer breakdown and eddy shedding. Little sound is produced during the early instability stages. Finally, §5 summarizes the major findings of this work.

2. Formulation

The continuity and momentum equations for a compressible flow can be combined to generate, in dimensionless form (Goldstein 1976),

$$\left[\left(\frac{\partial}{\partial t}+M\frac{\partial}{\partial X_1}\right)^2-\frac{\partial^2}{\partial X_j\partial X_j}\right]\rho=\frac{\partial^2 T_{ij}}{\partial x_i\partial x_j}, \tag{2.1}$$

where

$$T_{ij}=\rho\,(u_i-U_i)\,(u_j-U_j)+\frac{\delta_{ij}}{M^2}\left(\frac{p}{\gamma}-\rho\right)-\tau_{ij} \tag{2.2}$$

is the Lighthill stress tensor. It contains Reynolds stress defined in terms of the excess velocity relative to a uniform free-stream motion $U_i=(1,0,0)$, deviation from isentropy (the second term, where γ denotes the ratio of specific heats), and the viscous part of the Stokes stress tensor

$$\tau_{ij}=\frac{1}{Re}\left(\frac{\partial u_i}{\partial x_j}+\frac{\partial u_j}{\partial x_i}-\frac{2}{3}\delta_{ij}\frac{\partial u_k}{\partial x_k}\right). \tag{2.3}$$

In (2.1)–(2.3) the velocity components and the thermodynamic variables are non-dimensionalized with respect to the undisturbed free-stream values U'_∞, p'_∞ and ρ'_∞, respectively. The spatial coordinates are defined by $x_i=x'_i/L'_f$, where L'_f is a characteristic length scale of the flow field such as the boundary layer displacement thickness, and $X_i=Mx_i$. The latter, scaled relative to the characteristic acoustic wavelength, is introduced to facilitate the description of acoustic wave propagation.

Both x_i (y_i) and X_i will be used simultaneously throughout this paper to represent the near-field source region and the far-field observation points, respectively, bearing in mind that they are not independent of one another. The non-dimensional time, $t = t'U'_\infty/L'_f$, is the same for both acoustic and fluid dynamic disturbances. The Mach number is defined in terms of the equilibrium sound speed in the free stream, $M = U'_\infty/c'_\infty$; $c'_\infty = (\gamma p'_\infty/\rho'_\infty)^{1/2}$, and the Reynolds number is defined as $Re = U'L'_f/\nu'$.

Equation (2.1) is equivalent to a convective wave equation for a medium moving uniformly along the X_1 axis, if the right-hand side is viewed as distributed source terms. The source terms, typically dominated by the Reynolds stresses, are quadratically small outside the boundary layer because the unsteady motions there are purely acoustic. Within the disturbance region in the boundary layer, the source terms are treated as incompressible quantities, decoupled from compressible acoustic disturbances, on the basis that the latter are much smaller in magnitude. Thus, the flow noise issue is reduced to a problem of finding the solution to (2.1) under the appropriate boundary conditions, once the hydrodynamic field has been determined.

For a low-Mach-number flow, the proper scaling for the thermodynamic variables in the boundary layer is

$$p = 1 + M^2\tilde{p}, \qquad \rho = 1 + M^2\tilde{\rho}. \tag{2.4}$$

When these rescaled variables are used and terms of $O(M^2)$ or smaller are truncated, the governing equations for an ideal gas can be approximated by

$$\frac{\partial u_j}{\partial x_j} = 0, \tag{2.5}$$

$$\frac{\partial u_i}{\partial t} + u_j\frac{\partial u_i}{\partial x_j} = -\frac{1}{\gamma}\frac{\partial \tilde{p}}{\partial x_i} + \frac{1}{Re}\frac{\partial^2 u_i}{\partial x_j \partial x_j}, \tag{2.6}$$

$$\frac{\partial \tilde{s}}{\partial t} + u_j\frac{\partial \tilde{s}}{\partial x_j} = \frac{1}{PrRe}\frac{\partial^2 \tilde{s}}{\partial x_j \partial x_j} + \frac{\gamma - 1}{\gamma}\frac{1}{PrRe}\frac{\partial^2 \tilde{p}}{\partial x_j \partial x_j} + \frac{\gamma - 1}{Re}\Phi. \tag{2.7}$$

In (2.7) Φ denotes the dimensionless dissipation function, and the entropy, $\tilde{s} = \tilde{p}/\gamma - \tilde{\rho}$, is related to the second term in the Lighthill stress tensor (cf. (2.2)). Equations (2.5)–(2.7) suggest that it is only necessary to solve the incompressible version of the governing equations in order to evaluate the acoustic source terms. By using (2.4) and (2.5) in (2.1) and (2.2) and consistently ignoring the $O(M^2)$ terms, one can derive the approximate Lighthill stress tensor

$$T_{ij} \approx u_i u_j + \delta_{ij}\tilde{s} - \tau_{ij}. \tag{2.8}$$

The effect of entropy fluctuations in sound generation is generally negligible except under extreme conditions, such as in the presence of a strong temperature gradient or multi-phase flow (Crighton 1975). In the present case, it is insignificant given the reasonably large Reynolds number to be considered ($Re_{\delta^*} = 1000$). It is worth pointing out, however, that even in cases where entropy production is not negligible, its effect can be accounted for by solving the reduced energy equation (2.7) together with the incompressible Navier–Stokes equations, rather than resorting to a fully compressible numerical procedure. This can lead to considerable savings in computer resource.

The $O(M)$ convective term in the wave operator in (2.1) creates merely a small Doppler shift whose effect can be represented as a multiplicative correction (Lighthill 1993). If the bulk convection effect is ignored, (2.1) becomes the Lighthill equation

in a uniform acoustic medium at rest. Based on the result of Powell (Powell 1960; Crighton *et al.* 1992), its solution in the upper half-plane $X_2 \geqslant 0$ can be written as

$$4\pi[\rho(\boldsymbol{X},t)-1] = 2M^4\frac{\partial}{\partial X_\alpha}\int_S \frac{\tau_{\alpha 2}(\boldsymbol{y},t-|\boldsymbol{X}-M\boldsymbol{y}|)}{|\boldsymbol{X}-M\boldsymbol{y}|}\,\mathrm{d}^2\boldsymbol{y} + M^5\frac{\partial^2}{\partial X_i\partial X_j}\int_V \frac{T_{ij}(\boldsymbol{y},t-|\boldsymbol{X}-M\boldsymbol{y}|)}{|\boldsymbol{X}-M\boldsymbol{y}|}\,\mathrm{d}^3\boldsymbol{y} + M^5\frac{\partial^2}{\partial X_i^*\partial X_j^*}\int_V \frac{T_{ij}(\boldsymbol{y},t-|\boldsymbol{X}^*-M\boldsymbol{y}|)}{|\boldsymbol{X}^*-M\boldsymbol{y}|}\,\mathrm{d}^3\boldsymbol{y}, \tag{2.9}$$

where $\boldsymbol{X}^* = (X_1, -X_2, X_3)$ is the image of position $\boldsymbol{X}$ in the rigid surface $X_2 = 0$. Repeated indices i and j represent summmation over 1 to 3, whereas α and β are summed over 1 and 3 only. The two volume integrals represent a volume distribution of acoustic quadrupoles and their reflection in the rigid surface, respectively. They are evaluated over the entire unsteady flow region above the wall. The surface integral, evaluated on the wall, involves in-plane dipoles associated with the fluctuating surface shear stress, whose significance as a sound source is controversial. An overview of the shear stress controversy can be found in Crighton *et al.* (1992). The relative strengths of the volume and surface source terms depend upon the properties of the unsteady Reynolds stress and wall shear stress, in addition to the apparent Mach number scaling. Considerable simplification can be achieved in the far field under the condition that the source region is acoustically compact, as will be discussed in § 4.

3. Boundary layer simulation

3.1. *Background*

Transition to turbulence from a laminar boundary layer starts with a sequence of instability events, including two-dimensional (linear) primary instability and three-dimensional (nonlinear) secondary instability. Several paths to laminar breakdown, notably the fundamental and subharmonic (K- and H-type, respectively), have been identified through 'controlled' experiments (e.g. Klebanoff *et al.* 1962; Kachanov & Levchenko 1984). In the K-type breakdown the primary T-S wave and the secondary wave have the same streamwise wavelength. The secondary instability leads to the formation of a streamwise vortex system known as the lambda vortex, which in turn induces a detached high-shear layer on top. The high-shear layer intensifies, elongates, and develops instability. It breaks down gradually to generate smaller vortices, observed as velocity 'spikes'. The above K-breakdown scenario has been recorded in remarkable detail in recent experiments (Borodulin & Kachanov 1992; Kachanov 1994).

Numerical simulation of boundary layer transition based on the full Navier–Stokes equations requires enormous computer time and memory. As a result, the majority of simulations use the temporal formulation (e.g. Wray & Hussaini 1984; Spalart & Yang 1987; Zang & Hussaini 1987, 1990). In particular, the simulation of Zang & Hussaini (1990) provides a detailed description of both fundamental and subharmonic breakdown processes up to the two-spike stage. Spatial simulations are mostly limited to stages prior to breakdown (Fasel 1990; Fasel, Rist & Konzelmann 1990; Kleiser & Zang 1991), with the notable exception of Rai & Moin (1993). The latter study involves a relatively high level of free-stream turbulence, so that the

transition process does not necessarily follow the classical routes for small-amplitude T-S wave series. A comprehensive survey of pre-1991 literature is given by Kleiser & Zang (1991).

Gaster & Grant (1975) first directed attention to the effect of wave modulation in the transition process, which is essential to the formation of intermittency or turbulent spots observed in natural (uncontrolled) transition (Kachanov 1994). A number of experimental studies on modulated T-S waves are summarized in the review article by Kachanov (1994). The results indicate that only one or two periods of a wave are sufficient to cause resonant amplification, and that the nonlinear breakdown process within each wave packet proceeds in qualitatively the same way as in periodic wave series. The experiment by Gaster (1993) shows that amplitude modulation causes nonlinear amplification to occur at a much lower amplitude than in periodic wave series. At advanced stages of transition, high-frequency oscillations of 5–6 times the primary wave frequency are found to ride on the primary packet. These high-frequency bursts are identified with instabilities of the high-shear layer, and are the source of 'hairpin' vortices of finer scale.

Navier–Stokes simulations of wave packet transition in a boundary layer include, for example, those of Fasel (1990), Breuer (1990), and Henningson, Lundbladh & Johansson (1993). The initial disturbances used in these simulations consist of either a short-duration pulse excitation or a counter-rotating vortex pair. As a consequence, the transition processes are of 'bypass' type, skipping the T-S and secondary instability processes. Henningson, Spalart & Kim (1987) conducted direct simulations of turbulent spots in plane Poiseuille and boundary layer flows.

The numerical simulation carried out in the present work is focused on a strongly modulated T-S wave packet excited at the inflow boundary using a combination of two- and three-dimensional T-S eigenmodes for a short time duration. The simulation, based on a spatial formulation that allows the streamwise growth of the boundary layer, continues to the multiple-spike stage, just prior to turbulent spot formation. The laminar breakdown process is shown to follow closely the classical K-type, confirming earlier experimental observations (Kachanov 1994).

3.2. *Numerical method and boundary conditions*

In order to evaluate the acoustic sources arising from wave packet transition, (2.5) and (2.6) are solved using an incompressible Navier–Stokes solver developed by Le & Moin (1991). The equations are discretized using finite difference on a staggered grid, with uniform grid spacing in the streamwise (x_1) and spanwise (x_3) directions. In the wall-normal direction (x_2), non-uniform mesh is employed to allow grid refinement near the wall. Time advancement is of three-step Runge–Kutta type combined with a fractional step method. Each sub-step treats the convective terms explicitly and the viscous terms implicitly. The Poisson equation is solved at the final sub-step to satisfy the divergence-free constraint. The numerical scheme is second-order accurate in both space and time.

The domain of integration consists of a rectangular box parallel to the flow direction. The no-slip condition is applied on the solid wall surface. At the free-stream boundary 20 displacement thicknesses away from the wall, a normal velocity distribution based on the Blasius solution and zero vorticity are prescribed (notice that the normal velocity specification applies only to the near-field computation using the incompressible approximation; it by no means restricts the induced acoustic wave propagation to the far field, to be calculated separately). In the spanwise direction periodicity is assumed for all dependent variables.

The unsteady wave packet is introduced into the computational domain by imposing the following upstream boundary conditions:

$$u_i(x_1 = 0) = u_i^B(x_2) + \mathrm{Re}\Big\{ \epsilon^{2D} u_i^{2D}(x_2) \mathrm{e}^{\mathrm{i}\theta} \mathrm{e}^{-\mathrm{i}\beta t} + \tfrac{1}{2}\epsilon^{3D} u_i^{3D+}(x_2) \mathrm{e}^{\mathrm{i}[(\alpha \sin\phi)x_3 - \beta t]} + \tfrac{1}{2}\epsilon^{3D} u_i^{3D-}(x_2) \mathrm{e}^{\mathrm{i}[-(\alpha \sin\phi)x_3 - \beta t]} \Big\} \mathrm{e}^{-[(t-t_0)/\tau]^4} g(x_3), \tag{3.1}$$

where $u_i^B(x_2)$ represents the Blasius velocity for a two-dimensional boundary layer. Quantities $u_i^{2D}(x_2)$ and $u_i^{3D\pm}(x_2)$ are the least-stable eigenmodes and α is the corresponding eigenvalue, obtained by solving the Orr–Sommerfeld and Squire equations for given frequency β and oblique angle ϕ. The eigenfunctions are normalized such that the maximum streamwise velocity has unit magnitude. The same excitation frequency is applied to both two- and three-dimensional disturbances, which are separated in phase by angle θ. The streamwise extent of the wave packet is determined by the parameter τ in the time-modulating envelope. In addition, symmetry relative to the spanwise centre $x_3 = 0$ is destroyed deliberately by the function $g(x_3)$, whose explicit form will be given later. As pointed out by Corral & Jiménez (1991), spanwise asymmetry accelerates the transition process and renders the simulation more manageable.

At the downstream boundary, a convective boundary condition which takes advantage of the known base flow (Blasius solution) is implemented. It has the form

$$\frac{\partial u_i}{\partial t} + U_j \frac{\partial u_i}{\partial x_j} = U_j \frac{\partial u_i^B}{\partial x_j}, \tag{3.2}$$

where U_j denotes a prescribed characteristic velocity at the exit plane. $U_j = (1, 0, 0)$ for calculations presented in the present work. Equation (3.2) ensures that the steady solution converges to the laminar velocity profile, while disturbances are allowed to be convected out of the computational domain. In contrast, the convective outflow condition in its original form (Pauley, Moin & Reynolds 1988), which sets the right-hand side of (3.2) to zero, tends to distort the mean flow profiles and produce erroneous oscillations near the exit boundary (Wang 1993). These numerical errors can contaminate the sensitive acoustic source calculation, although their effect is relatively small if one is only concerned with the hydrodynamic quantities.

The time-dependent Navier–Stokes code has been subjected to several critical tests. It is shown to be capable of producing and maintaining steady-state solutions that are in excellent agreement with the Blasius solution. Additionally, it predicts correctly the linear amplification of two-dimensional T-S waves, in terms of both eigenmode shape and spatial growth rate, as compared with the result of linear stability theory.

3.3. *Flow structure during laminar breakdown*

The numerical simulation is carried out under the following conditions: $Re = 1000$, $\epsilon^{2D} = 0.025$, $\epsilon^{3D} = 0.01$, $\theta = 0$, $\phi = \pi/4$, $\beta = 0.094$, $\tau = 40$, $t_0 = 120$, and $g(x_3) = 1 + 0.1(\mathrm{e}^{-[(x_3 - 1.73)/1.73]^2} - \mathrm{e}^{-[(x_3 + 1.73)/1.73]^2})$. The reference length scale used to define Re and other dimensionless variables is the displacement thickness δ^* at the inflow boundary. The equivalent Reynolds number measured in terms of distance from the leading edge is $Re_x \approx 3.38 \times 10^5$.

Computations start on a $514 \times 130 \times 66$ grid covering a computational domain defined in $0 \leqslant x_1 \leqslant 200$, $0 \leqslant x_2 \leqslant 20$ and $-\lambda_{x_3}/2 \leqslant x_3 \leqslant \lambda_{x_3}/2$, where $\lambda_{x_3} \approx 25.95$ is the

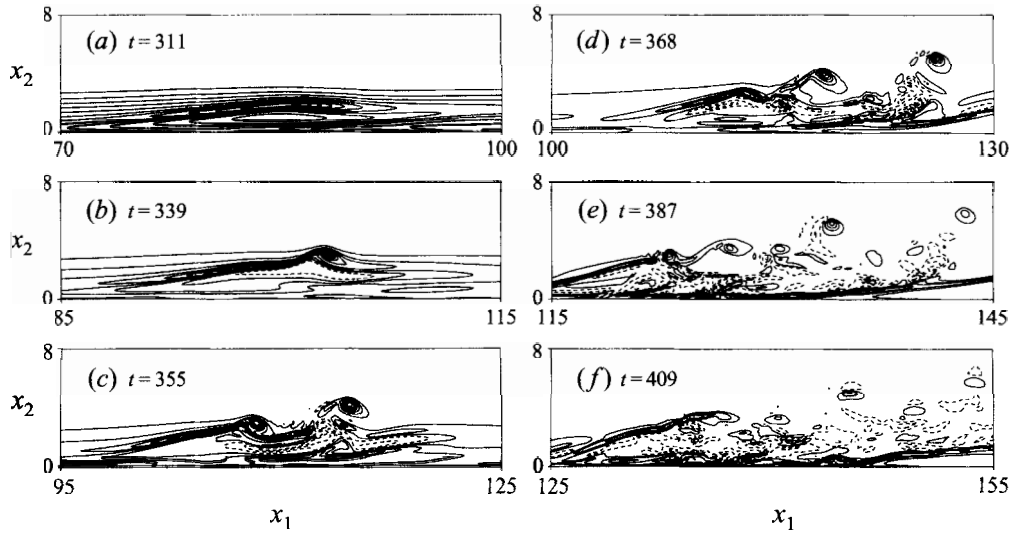

FIGURE 1. Contours of negative spanwise vorticity $-\omega_{x_3}$ at $x_3 \approx 1.1$ during laminar breakdown. Contour values: (*a*) 0 to 0.94; (*b*) −0.23 to 1.81; (*c*) −0.59 to 1.61; (*d*) −1.30 to 2.13; (*e*) −1.52 to 3.22; (*f*) −0.98 to 3.83.

spanwise wavelength for the oblique eigenmode pair. As the simulation proceeds, the resolution requirement becomes increasingly severe within the travelling disturbance region, whereas near the upstream boundary the flow becomes basically steady. Grid refinement is performed twice in conjunction with shifts in computational boundaries following the movement of the wave packet. A cubic-spline interpolation scheme is used to interpolate solutions onto new grids. When the downstream boundary of the new computational domain exceeds that of the old one, the grid point data in the extended region are initialized by interpolating a steady two-dimensional flow field computed earlier. By the end of the simulation, the computational grid consists of $1282 \times 130 \times 258$ points covering a shortened region $70 \leqslant x_1 \leqslant 210$. The entire simulation utilizes approximately 60 single-processor CPU hours on CRAY-C90.

Figure 1 depicts a time sequence of the instantaneous contours of the negative spanwise vorticity $-\omega_{x_3}$, which is closely related to the normal shear $\partial u_1/\partial x_2$, at $x_3 \approx 1.1$. Solid lines denote positive contour values, and dashed lines denote negative values. The plane $x_3 \approx 1.1$, which lies slightly off the spanwise centre, is chosen because it corresponds to the approximate location of maximum shear. In the interpretation of these results, it might be noted that due to the slight asymmetry of the initial T-S wave packet, the peak–valley splitting along the spanwise direction during the secondary instability is not as clear-cut as for symmetric disturbances. Nonetheless, the transition is seen to follow closely the route that leads to fundamental (*K*-type) breakdown.

The complete wave packet enters the upstream boundary $x_1 = 0$ at $t \approx 185$. Through the action of primary and secondary instability mechanisms, it amplifies rapidly, evolving into a detached high-shear layer as shown in figure 1(*a*). Underneath the shear layer lies a pair of counter-rotating streamwise vortices (lambda vortex) whose structure will be shown later. The high-shear layer intensifies to create a kink in figure 1(*b*), which breaks down in figure 1(*c*) to form a free vortex while a second kink develops. In figures 1(*d*)–1(*f*) the detached high-shear layer continues to disintegrate, shedding more eddies into the free stream. In the meantime, vortical

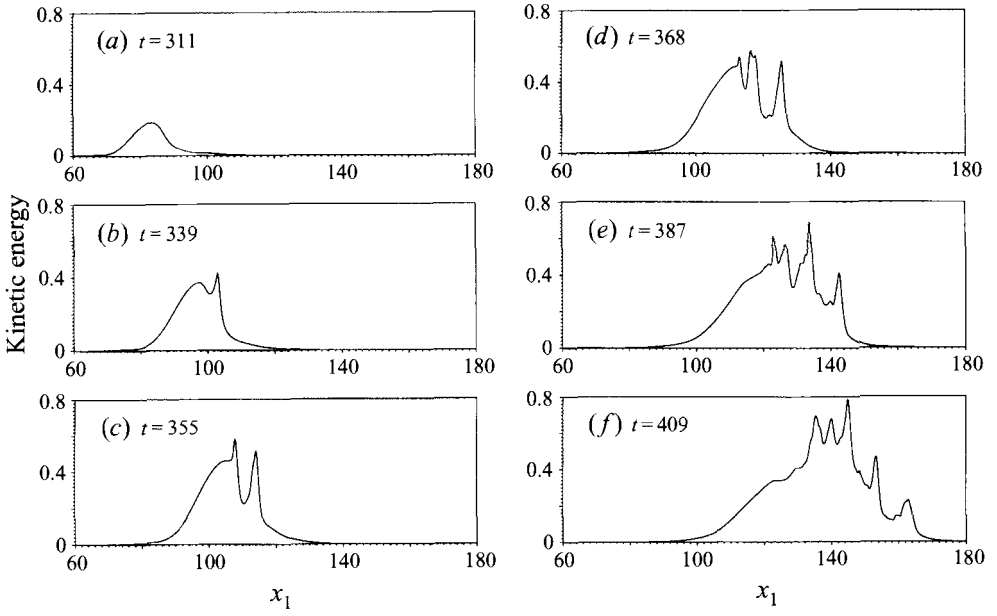

FIGURE 2. Evolution of disturbance kinetic energy integrated over the (x_2, x_3)-plane during laminar breakdown.

activity intensifies in the near-wall region, and a new generation of shear layers originates there. The new shear layers are expected to experience similar breakdown processes. The flow field depicted in figure 1(f) already bears a certain resemblance to turbulence. However, large-scale high-shear layers and streamwise vortices still dominate the overall flow structure, particularly in the rear part of the wave packet.

Figure 2 illustrates the streamwise distribution of the disturbance kinetic energy integrated over the (x_2, x_3)-plane, at time instants corresponding to those in figure 1. The kinetic energy is calculated based on the excess velocities relative to the steady flow solution. The snapshots show the nonlinear distortion of the energy waveform which leads to the formation of one, two and multiple spikes, each corresponding to a free eddy shed from the disintegrating high-shear layer. These spikes are observed in experiments concerning the K-regime breakdown (Kachanov 1994) as high-frequency flashes of disturbances on the streamwise-velocity oscilloscope traces. Kachanov notes that the velocity flashes do not disperse while they propagate downstream near the edge of the boundary layer, a feature identifiable with solitons. It is conceivable that the energy waveforms exhibited in figure 2 may be modelled by certain evolutionary equations within the framework of soliton theory. The spread of the nonlinear wave packet in the streamwise direction during laminar breakdown is apparent in figure 2. The amplitude increase observed in the energy waveform reflects not only the growth in disturbance velocities, but also the spread of the wave packet in the spanwise direction.

An interesting feature in the present simulation is the prescribed asymmetry relative to the spanwise centre. The asymmetry, albeit small at the beginning (10% relative to the overall wave amplitude), plays a significant role during the laminar breakdown process. The explicit effect of the spanwise asymmetry is illustrated in figures 3 and 4, which depict, respectively, the streamwise vorticity contours in selected x_2–x_3

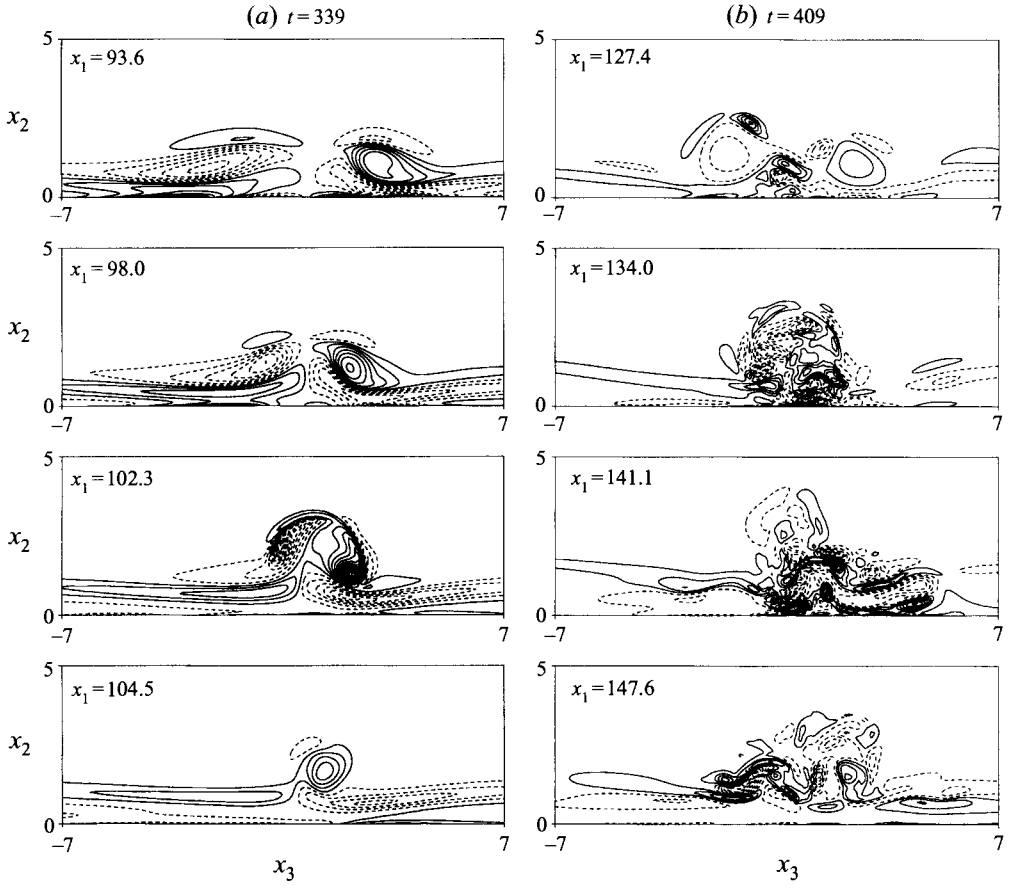

FIGURE 3. Streamwise vorticity contours at (*a*) $t = 339$ (contour spacing = 0.08); (*b*) $t = 409$ (contour spacing = 0.20).

cross-sections and the normal velocity contours in the plane $x_2 \approx 1.1$, at two time instants before and after laminar breakdown.

In figures 3(*a*) and 4(*a*) the two legs of the lambda vortex are seen to rise and merge gradually along the streamwise direction. The lambda vortex is 'crippled' in the sense that it has unequal strength in the two legs. The imbalance causes the two legs to become twisted near the tip of the vortex loop (cf. the third snapshot in figure 3*a*), accelerating the breakdown of the streamwise vortex structure and the high-shear layer supported by it. Similar observations have been made earlier by Corral & Jiménez (1991). This is in contrast to the case in which symmetry is imposed relative to the spanwise centre. A separate simulation conducted for a symmetric disturbance packet shows that the two vortex legs near the tip pinch together forcefully, stretch upwards, and push the high-shear layer farther into free stream. The transition process involves stronger-gradient transients that require a finer mesh to resolve. In addition, laminar breakdown takes place more slowly, resulting in increased simulation time.

By the time depicted in figures 3(*b*) and 4(*b*), the front portion of the primary lambda vortex structure has disintegrated, and regions of smaller streamwise vortices emerge. The disturbance region becomes elongated as the turbulence-like small-scale structures travel at a faster speed than the lambda vortex. At the rear the lambda vortex legs are still recognizable. Figures 3(*b*) and 4(*b*) also demonstrate that, up to

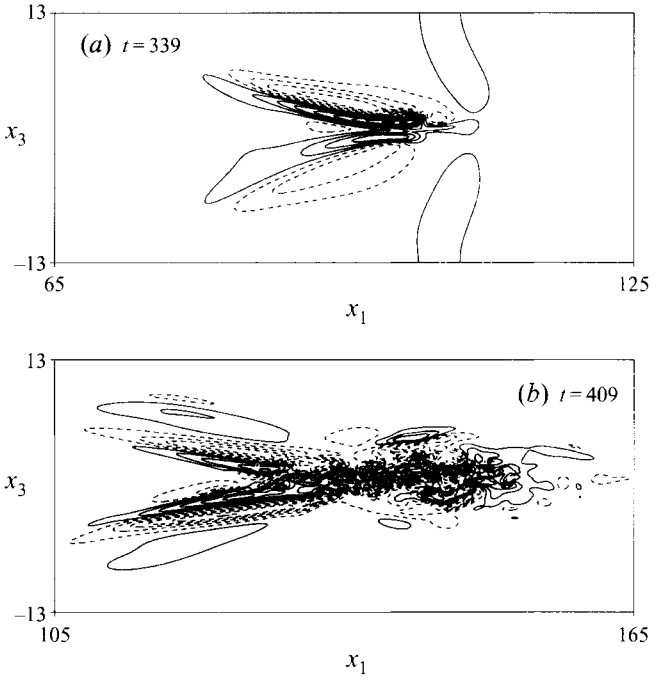

FIGURE 4. Contours of instantaneous normal velocity at $x_2 \approx 1.1$.
(*a*) $t = 339$, contour spacing = 0.015; (*b*) $t = 409$, contour spacing = 0.02.

this stage, the disturbance region remains small in the spanwise direction relative to the width of the computational box. Interaction between the neighbouring patches is negligible despite the periodicity imposed in the spanwise direction. Thus, the wave packet can be justifiably considered isolated.

The transition scenario described in this section is in qualitative agreement with experimental observations (Gaster 1993; Borodulin & Kachanov 1992). In particular, the coherent structures depicted in figures 1(*e*) and 1(*f*) are remarkably similar to the experimental measurements illustrated in figure 31 of Kachanov (1994). Quantitative comparisons are difficult because of a disparity in parametric conditions. The results of the present simulation are also in keeping with those of earlier numerical studies (Zang & Hussaini 1990; Kleiser & Zang 1991, for example). The latter are based on a temporal formulation (assuming streamwise periodicity) and do not exceed the two-spike stage. The observed similarity between the two types of simulations confirms that, as first suggested by Kachanov (1994), the laminar breakdown of a modulated wave packet proceeds in nearly the same way as that for a periodic T-S wave series. This illustrates the localized nature of resonant mechanisms that lead to laminar breakdown.

4. Acoustic radiation

4.1. *Volume contribution: computational considerations*

Acoustic computation based on Lighthill's theory is particularly simplified if the source is acoustically compact, i.e. if the region of unsteady flow is small in comparison to the emitted acoustic wavelength. The small retarded time variations in (2.9) can be approximated in the sense of multipole expansion, by expanding the integrands in

Taylor series about $t - |\boldsymbol{X}|$. Following this approach, the volume quadrupoles, which play an unambiguous role as a sound source, are examined first. A brief discussion of the viscous surface effects is deferred to §4.3.

In the low-Mach-number, far-field limit ($M \to 0$; $|\boldsymbol{X}| \to \infty$), the disturbance density arising from the two volume integrals in (2.9), henceforth denoted as ρ_v, can be approximated by

$$4\pi\rho_v(\boldsymbol{X}, t) \approx M^5 \frac{X_i X_j + X_i^* X_j^*}{|\boldsymbol{X}|^3} \ddot{Q}_{ij}(t - |\boldsymbol{X}|) \tag{4.1}$$

to leading order, where

$$\ddot{Q}_{ij}(t) = \frac{\partial^2}{\partial t^2} \int_V T_{ij}(\boldsymbol{y}, t) \mathrm{d}^3\boldsymbol{y} \tag{4.2}$$

gives the net quadrupole strength. This form is adequate for studying the acoustics of wave packet transition at low Mach number, because the size of the wave packet and that of the energy-containing coherent structures are $O(M)$ smaller than the acoustic wavelength. Since the compact quadrupole sources (4.2) do not contain retarded-time variations, they can be evaluated conveniently at each time step during the numerical integration of the Navier–Stokes equations.

In the subsequent calculations, the Lighthill stress tensor is approximated by the instantaneous Reynolds stress only. The viscous stress terms given by (2.3) are in fact of octupole nature because they involve an additional spatial derivative. As illustrated by Crighton (1975), these octupoles are $O(M^3)$ smaller in magnitude than the Reynolds stress quadrupoles. Clearly, the quadrupole formulation given by (4.1) and (4.2) is not appropriate for calculating the explicit volume viscous effects. Viscosity also contributes indirectly to the quadrupole noise sources through entropy generation caused by diffusive small-scale processes represented by the dissipation function Φ (cf. (2.7)). This effect is again small at relatively large Reynolds numbers (Crighton 1975) and is hence not evaluated.

If the source region is not compact, a more general method of computing the Lighthill analogy, based on (2.9) or its time-derivative form with full retarded time variations, must be employed. This requires formidably large amount of computer storage space if one desires the complete far-field solution. As a result, acoustic quantities are often evaluated at a limited number of observation points in a typical calculation. Useful techniques to account for the retarded time variations have been explored by, for example, Sarkar & Hussaini (1993) and Wang, Lele & Moin (1996).

A serious difficulty confronts computational acousticians when vortical structures enter or pass out of the computational domain, causing powerful spurious noise which may mask the true physical sound (Crighton 1993; Wang *et al.* 1996). This arises because, based on (4.1) and (4.2), the calculated sound signal is determined by the time derivatives of the total Lighthill stresses in the source region. If the entire disturbance region is not included in the finite computational domain, the time variations of the total Q_{ij} are dominated by the fluxes of T_{ij} across the integration boundaries, rather than by the internal generation of these quantities within the control volume.

Steps have been taken in order to eliminate the non-physical boundary effects. First, the computational boundaries for the Navier–Stokes simulation of the source field are maintained sufficiently far away from the region of significant disturbance, as is evident from a comparison of the computational box size ($140 \times 20 \times 25.95$) with the size of flow structures displayed in figures 1–4 (note that only part of the domain is plotted in each figure to magnify the main feature). This measure alone eliminates

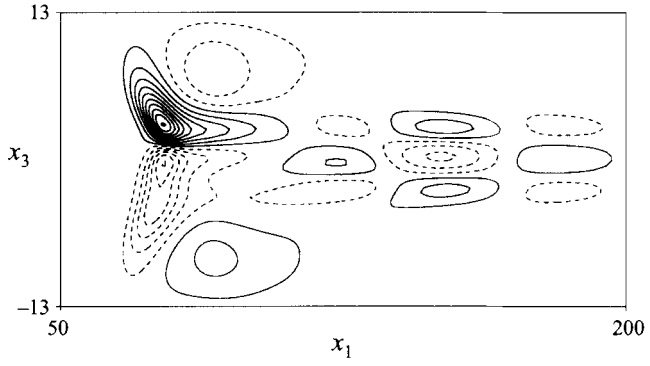

FIGURE 5. Contours of instantaneous normal vorticity at $x_2 \approx 2.3$, $t = 292$. Contour spacing = 0.0015.

most of the boundary errors at the expense of increased computational cost. However, it is not possible to keep all the disturbances away from the downstream boundary even if a very long computational domain is used. The difficulty is illustrated in figure 5, which depicts contours of the instantaneous normal vorticity at $x_2 \approx 2.3$, $t = 292$. The primary structure on the left is identified with the wave packet. The transient ripples induced by the wave packet extend all the way to the right because they are convected near the edge of the boundary layer at a faster speed.

The residual boundary effects caused by these ripples are removed by using a corrective formula derived by Wang *et al.* (1996),

$$\ddot{Q}'_{ij} = \ddot{Q}_{ij} + \dot{F}_{ij}, \qquad \dot{F}_{ij} = \frac{\partial}{\partial t}\int_S u_1^B T_{ij} \mathrm{d}^2 \boldsymbol{y}, \tag{4.3}$$

where the dots denote time derivatives, F_{ij} is the flux of Lighthill stress components, and S the downstream boundary of the source integration domain. Equation (4.3) assumes that T_{ij} is convected passively out of the outflow boundary at the local mean velocity. The approximation works well for the present problem, as demonstrated below, because the ripple disturbances are linear and travel at approximately the free-stream velocity.

Figure 6 illustrates the effect of boundary correction on $\ddot{Q}_{12}$, the component with the largest boundary influence. The dashed and dotted lines, representing the original quadrupole source and the time-derivative of the outflow boundary flux, respectively, show oscillations of similar magnitude but opposite phase for $t \leqslant 330$. As a result the corrected acoustic source (the solid line) remains nearly zero during this period. Had the spurious boundary contribution not been subtracted, one would predict incorrectly sound radiation when the wave packet transition is still in an early stage (cf. figure 1). At later times, figure 6 shows that the boundary flux contribution continues to be significant although the physical source gradually becomes dominant. The vertical dotted line in the figure indicates the time when the computational domain is reduced from $0 \leqslant x_1 \leqslant 200$ to $40 \leqslant x_1 \leqslant 180$ with higher resolution. This causes a discontinuity in $\ddot{Q}_{12}$ and $\dot{F}_{12}$, but $\ddot{Q}'_{12}$ remains continuous since the physical source is completely contained within both domains.

In what follows the prime in $\ddot{Q}'_{ij}$ is dropped to simplify notation, with the understanding that the quadrupole sources presented are free of boundary artifacts. Convergence of the source terms, including the surface shear stress terms to be presented later, is monitored by evaluating them in two domains of integration, whose

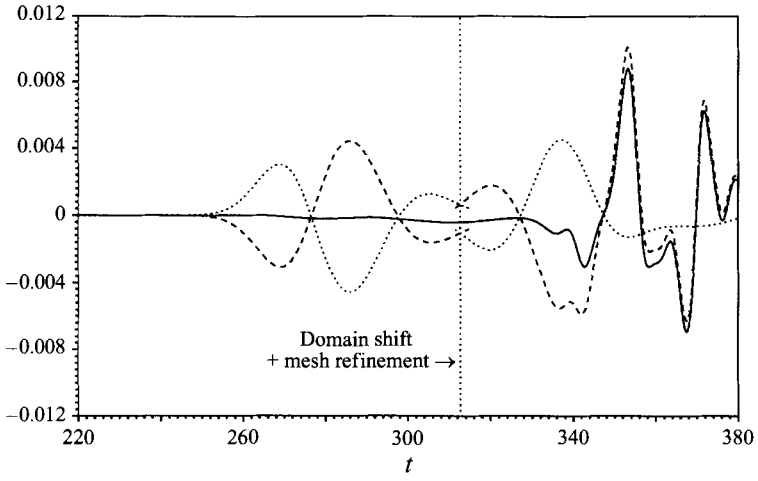

FIGURE 6. Time variation of a quadrupole source component, with and without boundary correction: ------, $\ddot{Q}_{12}$; ·····, $\dot{F}_{12}$; ——, $\ddot{Q}_{12} + \dot{F}_{12}$. The vertical dotted line denotes the time when a shift in computational domain and mesh refinement take place.

downstream boundaries are a short distance ($\sim$ 5 displacement thicknesses) apart. Agreement between the two solutions indicates that no boundary effect is present. As the wave packet approaches the outflow boundary, the two solutions begin to deviate, at which point the computational box is moved to a new downstream location.

4.2. *Volume contribution: numerical results*

Figure 7 illustrates the time variations of the net volume quadrupole terms $\ddot{Q}_{ij}$ calculated from (4.2) with the appropriate boundary corrections. Part (*a*) depicts the three longitudinal quadrupoles ($i = j$), and part (*b*) the lateral ones ($i \neq j$). Since the Lighthill stress tensor is symmetric, only six components are needed to define $\ddot{Q}_{ij}$ completely. The characteristics of source oscillations should be analysed in conjunction with the flow structures shown in figure 1. The quadrupole source signals generated by wave packet evolution are relatively weak initially, and then amplify dramatically as the shear layer begins to break down. Thereafter, the $\ddot{Q}_{ij}$ curves are seen to develop oscillations dominated by frequencies 5 to 7 times the basic T-S wave frequency (T-S wave period ≈ 66.5).

A close examination of the $\ddot{Q}_{11}$ curve and figures 1 and 2 indicates a strong correlation between source oscillation and vortex shedding in the boundary layer. At $t = 409$, the number of spikes (eddies) shown in figure 2 is approximately equal to the number of cycles experienced by $\ddot{Q}_{11}$. Thus it appears that the dominant mechanism for generating quadrupole sound is the intermittent vortex shedding resulting from strong inflexional instability of the high-shear layer. In his experiments with modulated T-S wave trains, Gaster (1993) observes bursts of secondary oscillations due to shear layer instability at 5 to 6 times the basic T-S wave frequency, coinciding with the dominant source frequencies calculated in the present study. Gaster further notes that the 'bursting' frequency is independent of the Reynolds number. The agreement between the frequency of shear layer instability and the acoustic source frequency further supports the assertion that the large-scale shear layer breakdown is primarily responsible for the calculated quadrupole sound.

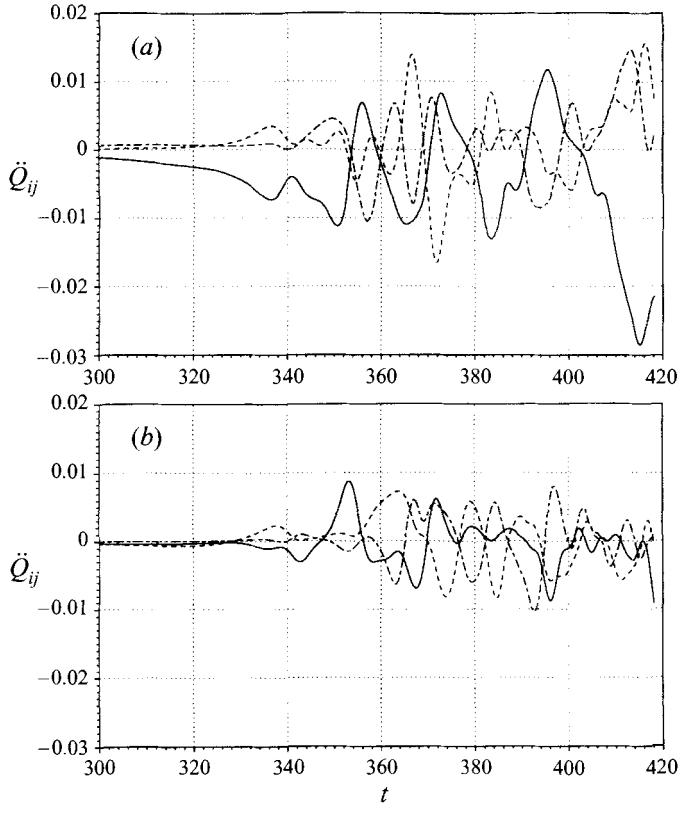

FIGURE 7. Time variations of volume quadrupole sources due to fluctuating Reynolds stress during laminar breakdown. (*a*) Longitudinal quadrupoles: ——— , $\ddot{Q}_{11}$; ------, $\ddot{Q}_{22}$; ---, $\ddot{Q}_{33}$. (*b*) Lateral quadrupoles: ——— , $\ddot{Q}_{12}$; ------, $\ddot{Q}_{13}$; ---, $\ddot{Q}_{23}$.

It is interesting to notice that no significant increase in higher frequency oscillations is observed in figure 7 as transition proceeds to create increasingly refined scales. Likewise, the amplitudes of $\ddot{Q}_{ij}$ remain basically invariant with time, even though the total kinetic energy of the source region (the area under each curve in figure 2) grows at an exponential rate. These observations can be explained in terms of the localized nature of shear-layer eddy shedding which dominates the instantaneous sound production. The small-scale features and the convected large eddies produced earlier are less efficient as quadrupole acoustic sources, although they contain large amount of disturbance energy.

One observes from figure 7 that the acoustic emission level is very low at the early stages of wave packet transition. At the earliest instant plotted ($t = 300$), the wave packet has already evolved into a lambda-vortex/high-shear-layer structure. To exemplify the behaviour of acoustic source terms during the primary and secondary instability phases of amplification, the longitudinal components of $\ddot{Q}_{ij}$ are depicted in figure 8 for $200 \leqslant t \leqslant 300$. They exhibit either monotonic growth or extremely low-amplitude oscillations at the basic T-S wave frequency (notice the different vertical scales used in figures 7 and 8). Other source terms behave in a similar fashion. Thus it can be concluded that linear and weakly nonlinear amplification of the T-S wave packet produces insignificant sound relative to the more violent breakdown processes later. Unfortunately, only the former regime is amenable to rigorous analytical

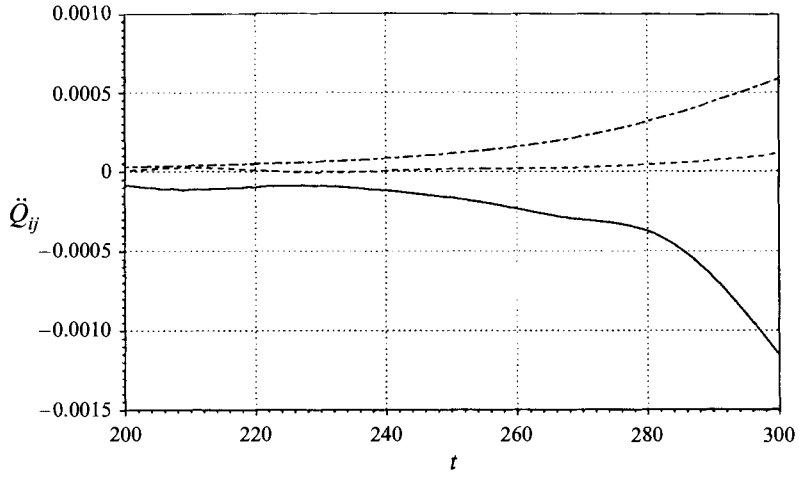

FIGURE 8. Time variations of longitudinal quadrupoles due to fluctuating Reynolds stress during instability stages. ——— , $\ddot{Q}_{11}$; ------, $\ddot{Q}_{22}$; – –, $\ddot{Q}_{33}$.

treatment (e.g. Ffowcs Williams 1967; Dolgova 1977; Akylas & Toplosky 1986; Haj-Hariri & Akylas 1986).

For flow-noise problems it is generally recognized that the energy-containing coherent structures provide the predominant noise source. The fine-scale structures associated with high-frequency phenomena are largely irrelevant (Crighton 1975), a conclusion supported by the lack of relatively high-frequency components in figure 7. To test the sensitivity of quadrupole sources to the size of flow structure, the computed flow field is filtered in (x_1, x_3)-planes using a box filter (Piomelli *et al.* 1991) of varying width before the volume integration in (4.2) is performed. The results for $\Delta_i = 2\Delta x_i$, $4\Delta x_i$, and $8\Delta x_i$, where Δ_i is the filter width in the i-direction ($i = 1$ and 3) and Δx_i is the mesh spacing, are compared in figure 9 with those without filtering. For brevity only the three longitudinal quadrupoles are given; the three lateral ones behave in the same way. Clearly, the basic source characteristics are preserved after filtering the flow field with a filter of widths up to $4\Delta_i$ ($2\Delta_i$ for $\ddot{Q}_{22}$). With a filter width of $8\Delta_i$, the results for $\ddot{Q}_{11}$ and $\ddot{Q}_{33}$ still show qualitative agreement with their unfiltered counterparts in terms of basic frequency and amplitude. This verifies that removing small-scale flow structures indeed has little impact on the distant-field sound radiation. Since the application of a box filter also alters the lower-wavenumber (large-scale) components to some extent, the actual agreement between unfiltered and filtered source quantities might be even better had the large-scale motion been precisely preserved.

The comparison made in figure 9 is also an indication of numerical convergence. It illustrates that the direct numerical simulation for the source field has adequately resolved the scales relevant to sound production. In fact, the simulation can be conducted on a coarser grid if the subgrid-scale stress can be modelled adequately. This suggests the promising role that can be played by the less-expensive large-eddy simulation methods for flow-noise prediction.

As an example, figure 10 depicts the distant sound field generated by the volume (Reynolds stress) quadrupoles in terms of iso-contours of the acoustic pressure p_v ($\equiv \gamma \rho_v$) at $X_3 = 0$ and $t = 420$. The source region is centred at $|\boldsymbol{X}| = 0$, bearing in mind that $\boldsymbol{X}$ is scaled relative to the acoustic length scale. The free-stream Mach number is $M = 0.02$, characteristic of underwater applications. The quadrupole

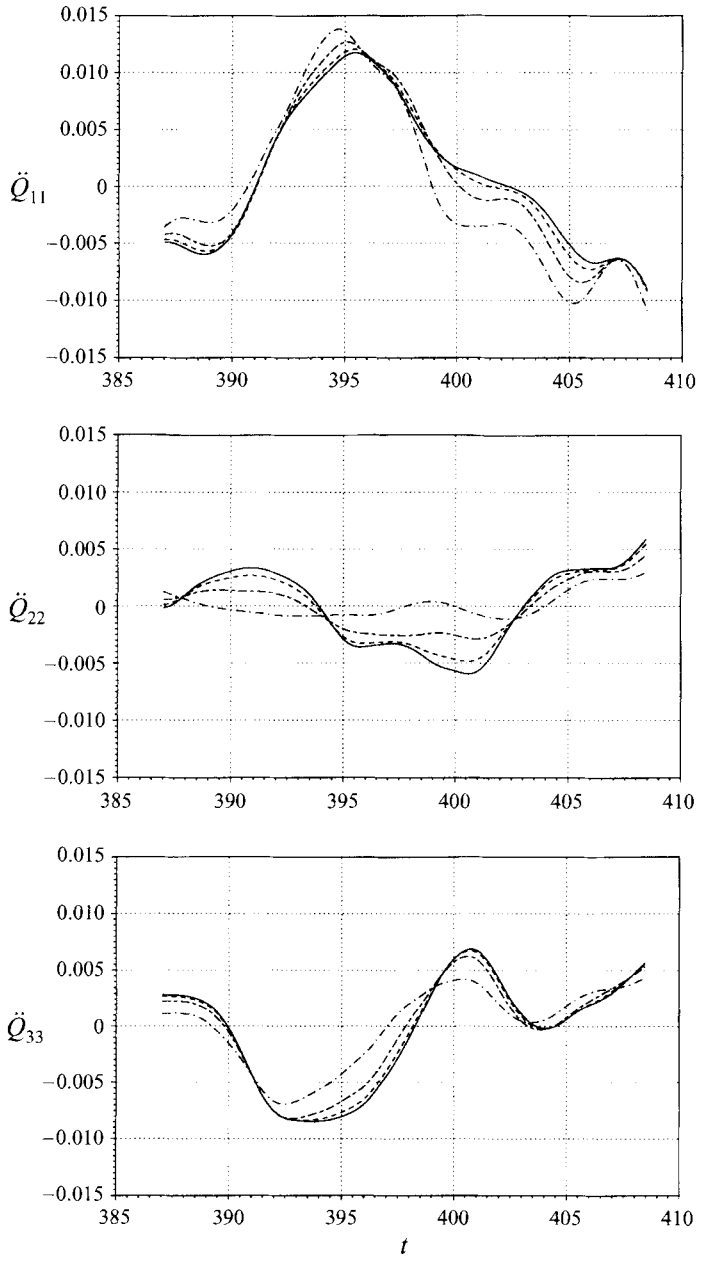

FIGURE 9. Longitudinal quadrupole sources calculated based on the velocity field filtered in the (x_1, x_3)-plane with filter width Δ_i. ——— , no filtering; ------ $\Delta_i = 2\Delta x_i$; – – – $\Delta_i = 4\Delta x_i$; -·-·-· $\Delta_i = 8\Delta x_i$.

radiation pattern suggests contributions from the longitudinal components but not the lateral ones. The latter are identically zero due to cancellations from wall reflection and the specific plane ($X_3 = 0$) selected for plotting (cf. (4.1)). It is worth pointing out that the extremely small contour values in figure 10 result from the M^5 factors in (4.1). In the present calculation, based on the acoustic analogy, sufficient arithmetic precision is maintained since the radiated pressure field is evaluated separately from

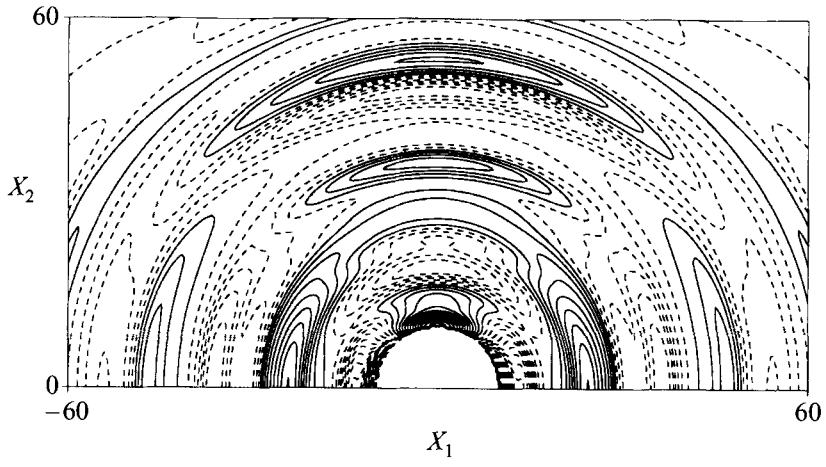

FIGURE 10. Iso-contours of the far-field acoustic pressure due to volume quadrupole radiation in the plane $X_3 = 0$ at $t = 420$. The free-stream Mach number $M = 0.02$. Contour levels from -1.02×10^{-12} to 0.50×10^{-12}.

the near-field computation. Given the huge disparity in acoustic and hydrodynamic magnitudes, a direct computation of acoustic radiation along with the source region using the compressible Navier–Stokes equations would be overwhelmed by computer round-off errors.

4.3. *Contribution from surface shear stress: an unsettled issue*

The interpretation to be placed on the surface integral in (2.9) has long been a subject of debate (Crighton *et al.* 1992). The central issue is whether the unsteady surface shear stress contributes to sound generation or is purely a propagation effect. If, following Landahl (1975), the wall shear stress is considered a generation term dominated by the hydrodynamic (non-acoustic) motion near the wall, the same multipole expansion procedure as for the volume sources can be invoked, and the surface shear stress contribution to the far-field density disturbance can be expressed in terms of net surface dipoles and quadrupoles. Numerical values of these compact surface source terms are documented in Wang, Lele & Moin (1994). Their magnitudes remain small during the shear layer lift-up and the generation of the first three spikes. As the laminar wave packet approaches the turbulent spot stage, however, the near-wall shear intensifies, giving rise to a surge in the dipole strength. Based on these results, and the Mach number scaling factors in (2.9), one would then conclude that at the late transition stage, the surface sound due to viscous stress fluctuations dominates the far field for a low-Mach-number flow, in agreement with Landahl (1975).

It should be emphasized, however, that the above result is based on the source data obtained from an incompressible simulation, as a leading-order approximation to the weakly compressible flow field. The validity of this treatment has been called into question in the low (supersonic)-wavenumber range, responsible for radiation to the distant field. As pointed out by Crighton *et al.* (1992), the shear stress $\tau_{\alpha 2}$ involves linear velocities and thus does not vanish even in the acoustic far field. Howe (1979) argues that the surface stress components at supersonic wavenumbers correspond to acoustic modes, and should be included in the propagation operator. Their effect, which actually causes diminished radiation, is found to be negligibly small at low Mach numbers except at the grazing angle. Howe's analysis does not

address the surface shear stress arising from the nonlinear hydrodynamic or turbulent motion, which has a significant low-wavenumber component as well, for the localized breakdown event considered here. Both the acoustic and hydrodynamic contributions are included in the analysis of Haj-Hariri & Akylas (1985), who conclude that the viscous shear stress dipoles also partake in sound generation. Their impact on the overall sound is found to be small for high-Reynolds-number flows because of a Re^{-1} factor. A definitive determination of the surface shear stress effect requires solutions to the compressible Navier–Stokes equations in a larger computational domain that covers both the transitional near field and the acoustic far field, which is beyond the scope of the present investigation.

This discussion is concluded with a historical note on a related linear 'source' term involving the normal stress, primarily the pressure. This term had been misinterpreted as a powerful dipole until Powell's (1960) discovery that the 'dipole' actually represents the specular image of the incident quadrupole system. The paradox is resolvable in the context of the Kraichnan–Phillips theorem (Kraichnan 1956; Phillips 1956; Howe 1992), which states that for an incompressible flow over a homogeneous plane boundary, the total normal force, and hence the 'dipole' strength must integrate to zero. Powell's reflection principle does not remove the surface shear stress dipoles, however, and there has been no direct proof, despite the suspicion, that an analogous situation exists concerning the shear stress terms. In the case of normal stress, each localized positive pressure spike is necessarily balanced by more extensive regions of negative pressure. Similar behaviour has not been observed for the hydrodynamic wall shear stress in the present calculation. A more thorough, rigorous investigation is needed to clarify this issue in a fundamental manner.

5. Summary

A computational study has been carried out concerning the sound emission from a localized disturbance, as it undergoes transition to turbulence in a boundary layer formed on a flat, rigid surface. The flow is characterized by small free-stream Mach number and a Reynolds number of 1000 based on the displacement thickness. Direct numerical simulation is applied in conjunction with the Lighthill acoustic analogy to determine the near-field flow dynamics and the far-field sound, respectively. The objectives are to establish a relationship between specific flow processes and the emitted acoustic signals, and to identify the primary noise source.

The boundary-layer disturbance initially consists of a modulated, three-dimensional T-S wave packet emulating that excited by free-stream turbulence in natural transition. Detailed accounts of the subsequent evolution, from the early linear stage to the final laminar breakdown, are obtained by solving the full incompressible Navier–Stokes equations. The simulation allows streamwise growth of the boundary layer thickness as well as spanwise asymmetry. The latter effect promotes interaction between the (unequal) lambda vortex legs and accelerates the high-shear layer breakdown and the associated eddy shedding. The route to turbulence is seen to follow the usual sequence of events for the fundamental breakdown type. The flow structures are in qualitative agreement with the experimental observations of Borodulin & Kachanov (1992).

Acoustic computation based on the Lighthill theory is facilitated by a multipole expansion in the compact source limit. The radiated far-field acoustic density (pressure) consists of contributions from volume and surface source functions due to the fluctuating Reynolds stress and the wall shear stress, respectively. The volume quadrupole sources produce negligible sound throughout the primary and secondary

instability processes of the wave packet. As the detached high-shear layer starts to disintegrate, dramatic amplification occurs to the volume quadrupole sound. The primary frequency (5–7 times the basic T-S wave frequency) of quadrupole radiation corresponds to the frequency of spike (eddy) generation in the near field, indicating the latter to be the physical source. The surface shear stress experiences a surge at a later breakdown stage as the disturbance region evolves to a turbulence spot. However, owing to the lack of compressibility effects in the source field data, the numerical results are inconclusive with regard to the role of the wall shear stress fluctuations in sound production. Further study is needed to elucidate this important aspect of boundary layer noise, perhaps by direct numerical simulation using compressible Navier–Stokes equations.

The authors are grateful to Drs K. Shariff and B. Mitchell for fruitful discussions during the course of this work, and to Professor G. M. Lilley for his careful reading of the manuscript and many helpful suggestions. Thanks are also due to Mr Y. Na for providing the original Navier–Stokes code, and to Mr S. Collis for providing the Orr–Sommerfeld eigensolver. Computations were carried out on the NAS facilities at NASA Ames Research Center. This project was supported in part by the Office of Naval Research under Grant N00014-92-J-1626. A preliminary version of this work was presented at the 1995 ASME Symposium on Flow Noise Modeling, Measurement and Control, NCA-19/FED-230, San Francisco.

REFERENCES

AKYLAS, T. R. & TOPLOSKY, N. 1986 The sound field of a Tollmien-Schlichting wave. *Phys. Fluids* **29**, 685–689.

BORODULIN, V. I. & KACHANOV, Y. S. 1992 Experimental study of soliton-like coherent structures. In *Eddy Structure Identification in Free Turbulent Shear Flows. IUTAM Symp. Poitiers, 1992.*

BREUER, K. S. 1989 The evolution of a localized disturbance in a laminar boundary layer. In *Laminar-Turbulent Transition* (ed. D. Arnal & R. Michel). *IUTAM Symp. Toulouse, France, 1989.* Springer.

CORRAL, R. & JIMÉNEZ, J. 1991 *Direct numerical simulation of the leading edge boundary layer. Tech. Note ETSIA/MF-916.* Dept. of Fluid Mech., Universidad Politécnica Madrid.

CRIGHTON, D. G. 1975 Basic principles of aerodynamic noise generation. *Prog. Aerospace Sci.* **16**, 31–96.

CRIGHTON, D. G. 1993 Computational aeroacoustics for low Mach number flows. In *Computational Aeroacoustics* (ed. J. C. Hardin & M. Y. Hussaini). ICASE/NASA LaRC Series, Springer.

CRIGHTON, D. G., DOWLING, A. P., FFOWCS WILLIAMS, J. E., HECKL, M. & LEPPINGTON, F. G. 1992 *Modern Methods in Analytical Acoustics*, Chap. 16. Springer.

CROW, S. C. 1970 Aerodynamic sound emission as a singular perturbation problem. *Stud. Appl. Maths* **49**, 21–44.

CURLE, N. 1955 The influence of solid boundaries upon aerodynamic sound. *Proc. R. Soc. Lond.* A **231**, 505–514.

DOLGOVA, I. I. 1977 Sound field radiated by a Tollmien-Schlichting wave. *Sov. Phys. Acoust.* **23**, 259–260.

FARABEE, T. M., HANSEN, R. J. & KELTIE, R. F. (eds.) 1989 *Flow-Induced Noise Due to Laminar-Turbulence Transition Process,* ASME NCA–Vol. 5, *ASME Winter Annual Meeting, San Francisco, 1989.*

FASEL, H. F. 1990 Numerical simulation of instability and transition in boundary layer flows. In *Laminar-Turbulent Transition* (ed. D. Arnal & R. Michel). *IUTAM Symp. Toulouse, France, 1989.* Springer.

FASEL, H. F., RIST, U. & KONZELMANN, U. 1990 Numerical investigation of the three-dimensional development in boundary layer transition. *AIAA J.* **28**, 29–37.

FFOWCS WILLIAMS, J. E. 1967 Flow noise. In *Underwater Acoustics*, Vol. 2, Chap. 6. Plenum.

GASTER, M. 1993 The origins of turbulence. In *New Approaches and Concepts in Turbulence* (ed. T. A. Dracos & A. Tsinober). Monte Verita Ser., Birkhauser, Boston.

GASTER, M. & GRANT, I. 1975 An experimental investigation of the formation and development of a wave packet in a laminar boundary layer. *Proc. R. Soc. Lond.* A **347**, 253–269.

GOLDSTEIN, M. E. 1976 *Aeroacoustics*, Chap. 4. McGraw-Hill.

HAJ-HARIRI, H. & AKYLAS, T. R. 1985 The wall-shear-stress contribution to boundary-layer noise. *Phys. Fluids* **28**, 2727–2729.

HAJ-HARIRI, H. & AKYLAS, T. R. 1986 Sound radiation by instability wave packets in a boundary layer. *Stud. Appl. Maths* **75**, 57–76.

HENNINGSON, D. S., LUNDBLADH, A. & JOHANSSON, A. V. 1993 A mechanism for bypass transition from localized disturbances in wall-bounded shear flows. *J. Fluid Mech.* **250**, 169–207.

HENNINGSON, D. S., SPALART, P. & KIM, J. 1987 Numerical simulations of turbulent spots in plane Poiseuille and boundary layer flow. *Phys. Fluids* **30**, 2914–2917.

HOWE, M. S. 1975 Contributions to the theory of aerodynamic sound, with application to excess jet noise and the theory of the flute. *J. Fluid Mech.* **71**, 625–673.

HOWE, M. S. 1979 The role of surface shear stress fluctuations in the generation of boundary layer noise. *J. Sound Vib.* **65**, 159–164.

HOWE, M. S. 1992 A note on the Kraichnan-Phillips theorem. *J. Fluid Mech.* **234**, 443–448.

KACHANOV, Y. S. 1994 Physical mechanisms of laminar-boundary-layer transition. *Ann. Rev. Fluid Mech.* **26**, 411–482.

KACHANOV, Y. S. & LEVCHENKO, V. Y. 1984 The resonant interaction of disturbances at laminar-turbulent transition in a boundary layer. *J. Fluid Mech.* **138**, 209–247.

KLEBANOFF, P. S., TIDSTROM, K. D. & SARGENT, L. M. 1962 The three-dimensional nature of boundary-layer instability. *J. Fluid Mech.* **12**, 1–34.

KLEISER, L. & ZANG, T. A. 1991 Numerical simulations of transition in wall-bounded shear flows. *Ann. Rev. Fluid Mech.* **23**, 495–537.

KRAICHNAN, R. 1956 Pressure fluctuations in turbulent flow over a flat plate. *J. Acoust. Soc. Am.* **28**, 378–390.

LAGIER, M. & SORNETTE, D. 1986 A two fluids model of the acoustic noise radiated by intermittent flow. *Acoustica* **61**, 116–123.

LANDAHL, M. T. 1975 Wave mechanics of boundary layer turbulence and noise. *J. Acoust. Soc. Am.* **57**, 824–831.

LAUCHLE, G. C. 1980 On the radiated noise due to boundary layer transition. *J. Acoust. Soc. Am.* **67**, 158–168.

LAUCHLE, G. C. 1981 Transition noise – the role of fluctuating displacement thickness. *J. Acoust. Soc. Am.* **69**, 665–671.

LAUCHLE, G. C. 1989 Transition as a source of radiated noise and vibration. In *Flow-Induced Noise due to Laminar-Turbulence Transition Process* (ed. T. M. Farabee, R. J. Hansen & R. F. Keltie). ASME NCA–Vol. 5, pp. 31–38.

LAUCHLE, G. C. 1991 Hydroacoustics of transitional boundary layer flow. *ASME Appl. Mech. Rev.* **44**, 517–531.

LAUFER, J., FFOWCS WILLIAMS, J. E. & CHILDRESS, S. 1964 Mechanisms of noise generation in the turbulent boundary layer. AGARDograph **90**, 39–50.

LE, H. & MOIN, P. 1991 An improvement of fractional step methods for the incompressible Navier–Stokes equations. *J. Comput. Phys.* **92**, 369–379.

LIGHTHILL, M. J. 1952 On sound generated aerodynamically; I. General theory. *Proc. R. Soc. Lond.* A **211**, 564–587.

LIGHTHILL, M. J. 1993 A general introduction to aeroacoustics and atmospheric sound. In *Computational Aeroacoustics* (ed. J. C. Hardin & M. Y. Hussaini). ICASE/NASA LaRC Series, Springer.

MARBOE, R. C. & LAUCHLE, G. C. 1992 Acoustic emissions from unsteady transitional boundary layer flow structures: theoretical model refinements. In *Flow-Structure and Flow-Sound Interactions* (ed. T. M. Farabee & M. P. Paidoussis), ASME NCA–Vol. 13, pp. 181–194.

MITCHELL, B. E., LELE, S. K. & MOIN, P. 1995 Direct computation of the sound from a compressible co-rotating vortex pair. *J. Fluid Mech.* **285**, 181–202.

MÖHRING, W. 1978 On vortex sound at low Mach number, *J. Fluid Mech.* **85**, 685–691.

PAULEY, L. L., MOIN, P. & REYNOLDS, W. C. 1988 A numerical study of unsteady laminar boundary layer separation. *Rep.* TF-34. Dept. of Mech. Engng, Stanford University.

PHILLIPS, O. M. 1956 On the aerodynamic surface sound from a plane turbulent boundary layer. *Proc. R. Soc. Lond.* A **234**, 327–335.

PIOMELLI, U., CABOT, W. H., MOIN, P. & LEE, S. 1991 Subgrid-scale backscatter in turbulent and transitional flows. *Phys. Fluids* A **3**, 1766–1771.

POWELL A. 1960 Aerodynamic noise and the plane boundary. *J. Acoust Soc. Am.* **32**, 982–990.

POWELL A. 1964 Theory of vortex sound. *J. Acoust Soc. Am.* **36**, 177–195.

RAI, M. & MOIN, P. 1993 Direct numerical simulation of transition and turbulence in a spatially evolving boundary layer. *J. Comput. Phys.* **109**, 169–192.

SARKAR, S. & HUSSAINI, M. Y. 1993 Computation of the acoustic radiation from bounded homogeneous flows. In *Computational Aeroacoustics* (ed. J. C. Hardin & M. Y. Hussaini). ICASE/NASA LaRC Series, Springer.

SORNETTE, D. & LAGIER, M. 1984 Acoustic noise radiated by transient flows. *Acoust. Lett.* **7**, 104–108.

SPALART, P. R. & YANG, K. S. 1987 Numerical study of ribbon-induced transition in Blasius flow. *J. Fluid Mech.* **178**, 345–365.

WANG, M. 1993 Sound radiation due to boundary layer transition. *Annual Research Briefs-1993*, pp. 299–312. Center for Turbulence Research, Stanford Univ./NASA Ames.

WANG, M., LELE, S. K. & MOIN P. 1994 Sound radiation during local laminar breakdown in a low mach number boundary layer. *CTR Man.* 153, Stanford Univ./NASA Ames.

WANG, M., LELE, S. K. & MOIN P. 1996 Computation of quadrupole noise using acoustic analogy. *AIAA J.*, submitted for publication.

WRAY, A. & HUSSAINI, M. Y. 1984 Numerical experiments in boundary layer stability. *Proc. R. Soc. Lond.* A **392**, 373–389.

ZANG, T. A. & HUSSAINI, M. Y. 1987 Numerical simulation of nonlinear interactions in channel and boundary layer transition. In *Nonlinear Wave Interactions in Fluids* (ed. R. W. Miksad, T. R. Akylas & T. Herbert). AMD Vol. 87, pp. 131–145. ASME.

ZANG, T. A. & HUSSAINI, M. Y. 1990 Multiple paths to subharmonic laminar breakdown in a boundary layer. *Phys. Rev. Lett.* **64**, 641–644.